Nanoscale Ion Transport Enhances Conductivity in Solid Polymer-Ceramic Lithium Electrolytes

Georgios Polizos[a], Monojoy Goswami[b], Jong K. Keum[c,d], Lilin He[c], Charl J. Jafta[a], Jaswinder Sharma[a], Yangyang Wang[d], Logan T. Kearney[b], Runming Tao[a], Jianlin Li[a]**

a. Electrification and Energy Infrastructures Division, Oak Ridge National Laboratory, Oak Ridge, TN 37831, USA

b. Chemical Sciences Division, Oak Ridge National Laboratory, Oak Ridge, TN 37831, USA

c. Neutron Scattering Division, Oak Ridge National Laboratory, Oak Ridge, TN 37831, USA

d. Center for Nanophase Materials Sciences, Oak Ridge National Laboratory, Oak Ridge, TN 37831, USA

KEYWORDS: Polymer electrolyte, lithium bis(trifluoromethanesulfonyl)imide (LiTFSI), lithium bis(fluorosulfonyl) imide (LiFSI), aluminum substituted lithium lanthanum zirconium oxide, Solid state batteries.

ABSTRACT: The predictive design of flexible and solvent-free polymer electrolytes for solid-state batteries requires the understanding of the fundamental principles governing the ion transport. In this work, we establish a correlation between the composite structures, polymer segmental dynamics and lithium ion (Li^+) transport in a ceramic-polymer composite. Elucidating this structure-property relationship will allow tailoring the Li^+ conductivity by optimizing the macroscopic electrochemical stability of the electrolyte. The ion dissociation from the slow polymer segmental dynamics was found to be enhanced by controlling the morphology and functionality of the polymer/ceramic interface. The chemical structure of the Li^+ salt in the composite electrolyte was correlated with the size of the ionic cluster domains, the conductivity mechanism, and the electrochemical stability of the electrolyte. Polyethylene oxide (PEO) filled with lithium bis(trifluoromethanesulfonyl)imide (LiTFSI) or lithium bis(fluorosulfonyl) imide (LiFSI) salts was used as a matrix. A garnet electrolyte, aluminum substituted lithium lanthanum zirconium oxide (Al-LLZO) with planar geometry was used for the ceramic nanoparticle moieties. The dynamics of the strongly bound and highly mobile Li^+ were investigated using dielectric relaxation spectroscopy. The incorporation of the Al-LLZO platelets increased the number density of the more mobile Li^+. The structure of the nanoscale ion-agglomeration was investigated by small angle X-ray scattering while molecular dynamics (MD) simulation studies were conducted to obtain the fundamental mechanism of the decorrelation of the Li^+ in the LiTFSI and LiFSI salts from the long PEO chain.

INTRODUCTION

Solid-state batteries (SSBs) are one emerging technology for energy storage with a potential for high energy density and superior safety. Realizing SSBs requires development in both material discovery and processing. Fabricating SSBs especially with ceramic electrolyte remains challenging.[1] From material processing perspective, polymer electrolytes could be a near-term solution to manufacture SSBs due to their flexibility, roll-to-roll processing, and excellent interfacial properties.[2,3] To this end, it requires the design of next-generation lightweight, flexible, solvent-free, and electrochemically stable polymer electrolyte materials with ultrafast and well-defined ion transport properties (conductivity values 10^{-4} to 10^{-3} S cm^{-1}, and transference number higher than 0.5).[2] Tailoring the nanostructure-property interdependencies associated with the ion transport is a viable approach toward the predictive design of polymer electrolytes with ultrahigh conductivity. The ion transport can be quantitatively expressed by three basic transport parameters: the ion mobility, the free ion concentration, and the transference number.[4] To tailor these parameters several electrolyte architectures have been proposed and investigated.[5-11] Among the vast structural variability of the studied electrolytes, representative electrolyte types are related to single-ion conductors, cross-linked, gel, plasticized, nanostructured block copolymers and composite electrolytes.[12-19] Each type has significant advantages and disadvantages. For example, the single-ion polymer electrolytes possess the unique advantage of ion transference number close to unity[20] where the anions are covalently bonded to the polymer backbone and the free ions (cations) transport through the polymer chains.[4] This configuration enables high transference numbers, can also utilize multifunctional groups along the polymer backbone but suffers from low conductivity values. Gel electrolytes exhibit high conductivity values at room temperature and may also be in-situ polymerized in a battery assembly; however, their dendrite resistance is poor and passive filler material such as glass fibers are typically used to enhance their electrochemical stability and critical current density.[21] Among the different electrolyte types, polymer composite electrolytes commensurate property advantages from both phases. The ceramic oxide phase is highly conductive and dendrite resistance whereas the polymer phase, although less conductive, provides a flexible and easily processable matrix for dispersing the ceramic phase and synthesizing a standalone thin film electrolyte with excellent interfacial properties with the cathode and the anode. The structure-property interdependencies between the ceramic phase and the ionic transport mechanism is still an intriguing concept in composite polymer electrolytes for SSBs.

In that respect, the focus of this work is to elucidate the fundamental principles of nanoscale Li^+ motion that govern the Li^+ ion transport and conductance at mesoscale in polyethylene oxide (PEO) electrolyte filled with lithium bis(trifluoromethanesulfonyl)imide (LiTFSI) or lithium bis(fluorosulfonyl) imide (LiFSI) salts. To further enhance Li^+ transport, a garnet-type electrolyte, aluminum substituted lithium lanthanum zirconium oxide (Al-LLZO) was used for the ceramic phase. Focusing on the PEO/Al-LLZO interfacial properties, the Al-LLZO fillers were synthesized with planar geometry. This configuration resulted in a better adsorption of the PEO segments on the surface of the Al-LLZO. At this interface, the Li^+ ion motion is highly correlated at the nanoscale that affect the mesoscopic transport mechanism due to the strong coupling between the Li^+ and the PEO, the formation of cationic and anionic ionic cluster domains (due to the high salt loading), and the presence of ionically conducting ceramic interfaces. The nanoscale diffusion of the Li^+ ions may take place through the PEO segmental motion (coordination to the PEO oxygen atoms), or through an interfacial diffusion at the Al-LLZO/PEO boundaries, or through a diffusion process within a salt cluster (intra-cluster diffusion) or among adjacent clusters (inter-cluster diffusion).[22-24] To establish the design parameters that govern the macroscopic properties of a SSE with respect to the SSB performance, it is essential to understand the mesoscale transport properties. The latter are inevitably dependent on a synergistic combination of the nano- and meso-scale transport mechanisms.

In this work, the molecular mechanisms at the nanoscale responsible for the long-range conductivity were investigated. Li^+ ions in SSE may exist in different phases such as ions that are strongly bound to their coordination sites, ions that are loosely bound to the coordination sites and free ions that participate in the long-range conductivity mechanism.[25,26] The number density of the different states depends on the electrostatic interactions between the Li^+ ions and the coordination sites. To design ultrafast ionic interfaces, it is essential to delineate the mechanism responsible for optimizing the number density of the free and more mobile ions. In this study, we show that by tuning the morphology and functionality of the polymer/ceramic interface, the Li^+ ions can dissociate (decouple) from the local polymer environments and diffuse over long-range macroscale domains. The dynamics of the polymer segment rearrangements (cooperative dynamics) responsible for the facilitation of the conductivity mechanism are very slow and prohibit the fast ion transport through the polymer phase. A thermodynamically favorable coordination of the ions to the Li^+ conductive ceramic interfaces will enhance the long-range migration of the ions. The dynamical interfacial processes were quantitatively analyzed using dielectric relaxation spectroscopy. The LiTFSI and LiFSI are two of the most typical salts used in SSEs. The correlation between their chemical structure and the conductivity mechanism was studied extensively. The formation of ionic cluster domains in the bulk structure of the electrolyte was correlated with the chemical structure of the Li^+ salts and the size of these clusters was estimated from small-angle X-ray scattering (SAXS) measurements. Molecular dynamics (MD) simulation studies were used to model the Li^+ ion transport mechanism with respect to the PEO segmental motion and the formation of the ionic cluster domains. This work focuses on the fundamental understanding of the correlations between motional processes with different time and length scales that superimpose and dictate the Li^+ ion conductivity mechanism. The conductivity mechanism was correlated with the electrochemical stability of the electrolyte to identify the design principles that govern the Li^+

ion conduction process in polymer electrolyte materials with tailored ionic conductivity and electrochemical stability for SSBs.

RESULTS AND DISCUSSION

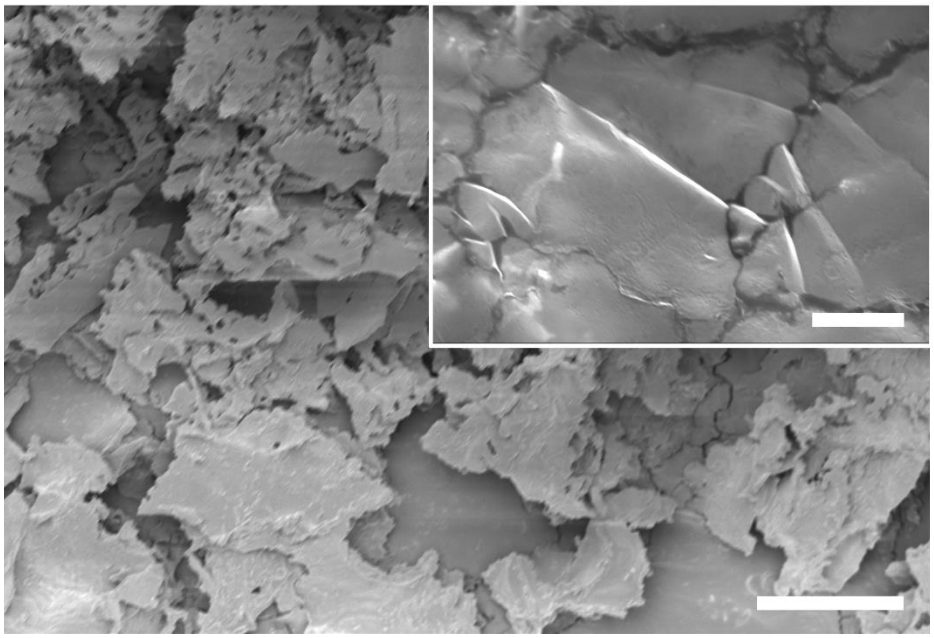

Figure 1. SEM image of the electrospun Al-LLZO platelets. The scale bar is 10 μm. The inset shows a cross-sectional SEM image of a composite PEO electrolyte filled with 15 wt% Al-LLZO. The scale bar is 4 μm.

The morphology of the electrospun Al-LLZO platelets is shown in Figure 1. Although their lateral dimensions are several micrometers, the platelets are sub-micrometer in thickness. The planar configuration is expected to provide enhanced resistance against the formation of Li^+ dendrites, result in a better adsorption of the polymer electrolyte on the surface of the ceramic electrolyte Al-LLZO and facilitate the self-assembled configuration of Al-LLZO/PEO structures during the drying process of the electrolyte. A cross-sectional SEM image of a composite PEO electrolyte filled with 15 wt% Al-LLZO is shown in the inset of Figure 1 (EDX analysis of the cross-sectional image as well as additional SEM images of the top and side view of the electrolyte are provided in Figures S16 and S17). A stack of assembled sub-micrometer thick Al-LLZO platelets is evident in the image. The planar geometry and the large surface size of the fillers is expected to induce an interfacial conductivity mechanism through interconnected or adjacent Al-LLZO platelets.

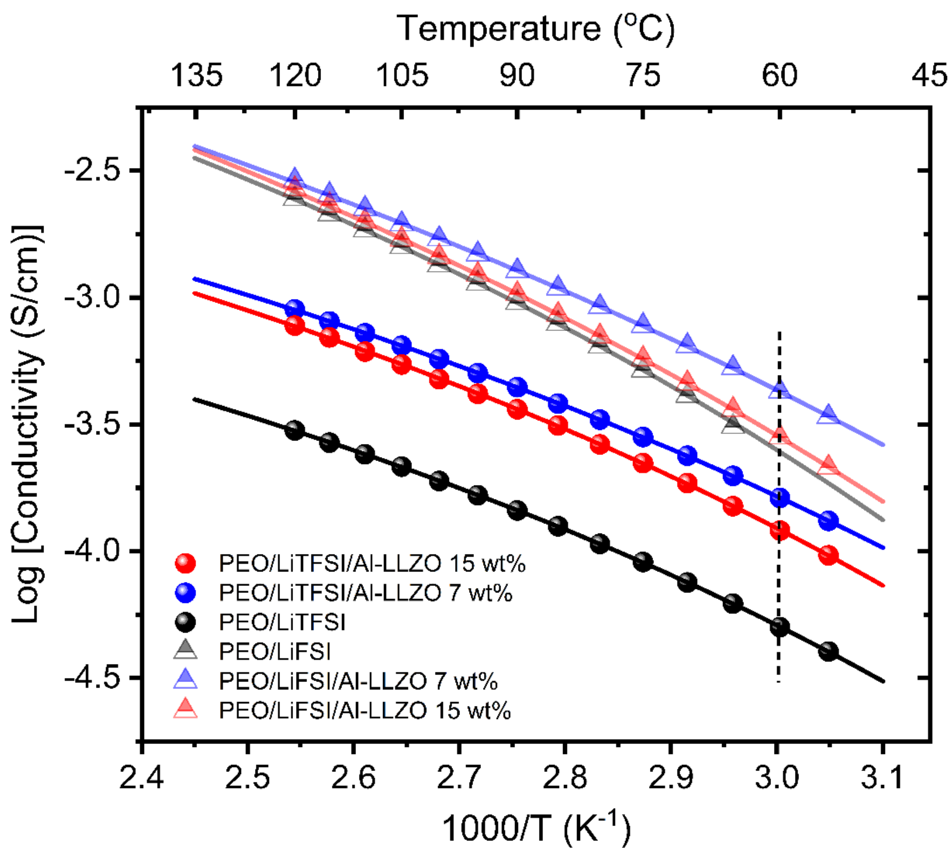

Figure 2. Summarized Arrhenius plot for the composite LiTFSI and LiFSI PEO electrolytes filled with Al-LLZO. The electrochemical testing was performed at 60 °C (dotted line on the plot).

The Li^+ ion conduction mechanism is a synergistic motion that can be correlated with the bulk polymer phase and the polymer/ceramic interfaces. It can be facilitated through the segmental motion of PEO amorphous domains, ion-hopping tangentially along the surface of the dispersed Al-LLZO platelets.[27,28] To study the conductivity mechanism of the composite LiTFSI and LiFSI electrolytes, DRS measurements were performed. In Figure 2, the conductivity measurements show that the pristine PEO/LiFSI electrolyte is more conductive than the PEO/LiTFSI electrolyte.[29] The transference numbers[30] were calculated from the diffusion coefficients in the MD simulations and are shown in Figure S13. The higher transference number of the LiFSI electrolyte is consistent with the higher conductivity values in Figure 2. The Al-LLZO composite with LiTFSI and LiFSI electrolytes are more conductive than the respective pristine electrolytes in the entire temperature range. Furthermore, Al-LLZO/LiFSI composites are more conductive than the Al-LLZO/LiTFSI. In both systems (LiTFSI and LiFSI) the 7 wt% composite exhibits the highest conductivity. This optimum filler concentration can be related to a better filler distribution due to the large size of the Al-LLZO fillers and their planar geometry. The temperature dependence of the conductivity values was fitted with the Vogel-Fulcher-Tammann (VFT) equation,

$$\sigma_{dc}(T) = \sigma_0 exp\left(-\frac{B}{T-T_0}\right) \qquad (1)$$

, where, σ_0, B, and T_0, are temperature independent parameters. σ_0 denotes the conductivity value in the high temperature limit, B can be used to calculate the pseudo activation energy (change of slope of the fitting curve as a function of temperature), and T_0 is a temperature that is dependent on the glass transition temperature (it is close to the ideal glass transition temperature which is approximately 50 K lower than the thermodynamic glass transition temperature, T_g). The fitting parameters as well as the conductivity values of the electrolytes at 60 °C are summarized in Table S1 in the Supporting Information. Above the melting temperature of the (PEO)–Li^+ complexes (or above the T_g for non-crystalline polymers) the conductivity is typically described by a VFT dependence, which indicates that ionic transport is governed by the disentangled motion of the polymeric chains resulting in ion-hopping from cluster to cluster (inter-cluster diffusion). Currently, the most common performance limitations in polymer electrolytes are linked to the ion mobility and free ion concentration, which are limited by the slow segmental motion and poor solvation properties of the polymer host as well as by the formation of strongly aggregated crystalline domains.[31-33] In the 50 – 100 ºC temperature range above T_g, ionic transport occurs only when the local conformations of the polymeric chains (segmental motion) enable the uncorrelated ion interstitial motion. Furthermore, The VFT curves of the LiTFSI with Al-LLZO (red/blue sphere) composites in Figure 2 are parallelly shifted to higher conductivity values compared to the pristine PEO/LiTFSI electrolyte (black sphere). The VFT dependence of the LiFSI electrolytes is significantly different, i.e., the conductivity values merge in the high temperature limit and decouple at lower temperatures. This distinctively different conductivity mechanisms are also evident in the different *B* parameter fitting values of the LiTFSI and LiFSI electrolytes (Table S1). The apparent activation energies of the conductivity mechanism are shown in Figure S19. The variation of the E_{app} values showed a weaker dependence with temperature for the composite electrolytes indicating a synergistic ion transfer mechanism through the segmental polymer phase (VFT-type) and through the Al-LLZO platelets (Arrhenius-type).[34] To further investigate the conductivity mechanism, a comparison of the dielectric loss spectra was performed at 60 ºC (operating temperature of the electrolytes) and the analysis results were compared with structural (SAXS) and MD simulation studies.

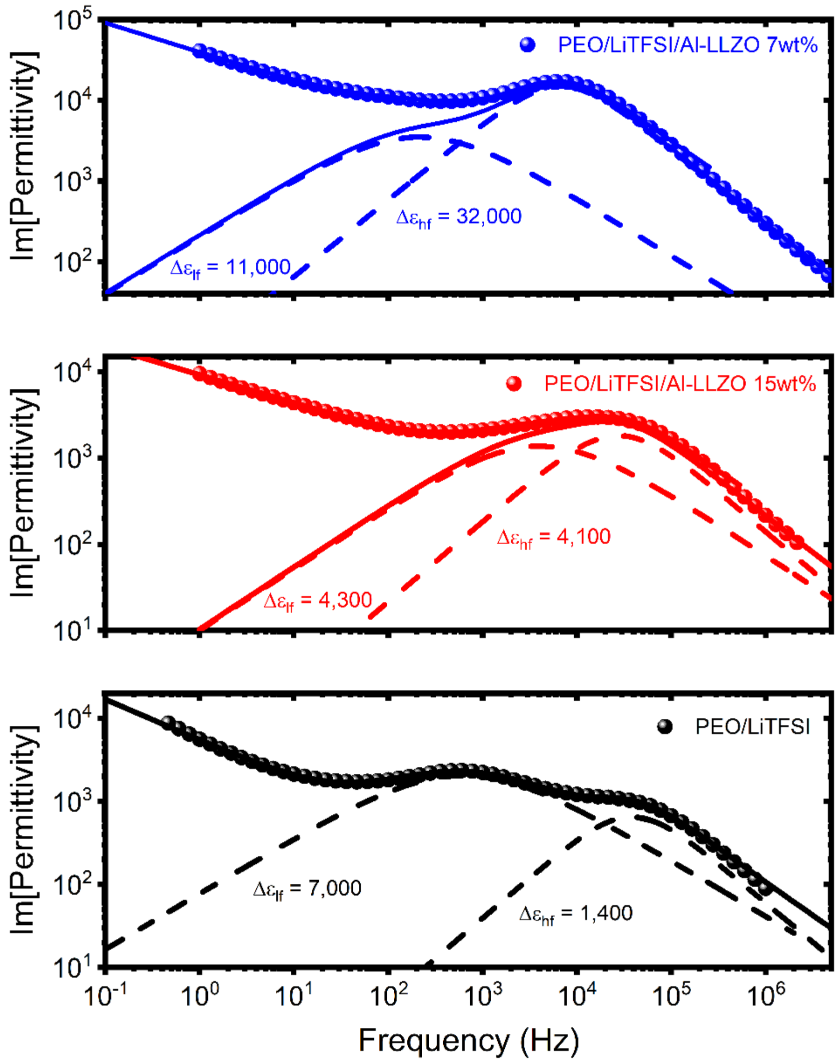

Figure 3. Dielectric loss spectra and fitting analysis of the pristine PEO/LiTFSI electrolyte and the 7 and 15 wt% Al-LLZO composite electrolytes at 60 °C. The solid lines are the best fitting of Eq. 3 to the experimental data. The dashed lines correspond to the two relaxation processes according to the fitting analysis. The calculated relaxation strengths for the low frequency ($\Delta\varepsilon_{lf}$) and high frequency ($\Delta\varepsilon_{hf}$) processes are also indicated on the plots.

A comparison plot of the imaginary part of the permittivity function for the LiTFSI electrolytes at 60 °C is shown in Figure 3. The pristine PEO/LiTFSI electrolyte is characterized by a bimodal relaxation mechanism and a low frequency power law contribution due to conductivity and polarization effects. Least-square fitting analysis to the dielectric spectra was performed by using a superposition of two Havriliak-Negami (HN) expressions and a power law contribution to simulate the low frequency conductivity process.[35-37] The permittivity analysis method is described in the Experimental section. The low and high frequency peaks of the pristine PEO/LiTFSI electrolyte in Figure 3 correspond to mechanisms with slower and faster dynamics, respectively (the relaxation time is inversely proportional to the frequency). According to the fitting analysis, the exponent s in Eq. 3 was found to be lower than 1 indicating that the low frequency power law contribution is due to bulk polarization effects.[36] Considering the high values of the dielectric losses and the absence of relaxation mechanisms in that frequency range for the PEO without LiTFSI salt (Figure S2), the two relaxation mechanisms can be attributed to polarization processes due to the dispersed Li^+ ions and the induced dipole moments in the bulk structure of the electrolyte. The time scales of these two processes follow a VFT dependence (Figure S3) indicating a conductivity mechanism dependent on the slower segmental dynamics of the PEO. Therefore, the relaxation with the slower dynamics can be associated with the less mobile Li^+ (i.e., strongly bound to the PEO polymer chain), whereas the relaxation with the faster dynamics can be associated with dispersed Li^+ ions that are more mobile. The relaxation strength is a measure of the number density of the relaxing units that contribute to the relaxation process. A change in the ratio of the $\Delta\varepsilon$ values of the two measured relaxation processes would be directly related to the relative change in the number density of the respective relaxing units. The dielectric spectra analysis of the PEO/LiTFSI in Figure 3, show two well separated peaks in the low and high frequency ranges. The relaxation strength of the slower relaxation is five times higher than that of the faster relaxation at the higher frequency range. This dynamical behavior correlates well with the macroscopic conductivity values. Among all electrolytes, the lowest conductivity values of the pristine PEO/LiFTSI electrolyte (Figure 2) can be associated with the increased number density of the less mobile (strongly bound) Li^+ ions and the less correlated motion between the strongly bound and the more mobile Li^+ ions (the f_{max} of the peaks are approximately two orders of magnitude separate in the frequency domain indicating motions with very different time scales). The dispersion of Al-LLZO fillers resulted in a significant different dynamical behavior. The 15 wt% composite is more conductive than the pristine electrolyte. The relaxion strength of the high frequency mechanism increased and became almost equal to that of the low frequency mechanism suggesting an increased ratio between the more mobile and the less mobile ions. Moreover, the two processes are now closer positioned. The more pronounced overlapping may also indicate higher degree of correlated motion between the Li^+ ions with PEO segmental dynamics and an easier transition between the strongly bound and the more mobile states. Similar dynamical behavior is observed for the most conductive 7 wt% electrolyte. The relaxation strength of the faster Li^+ ions is approximately three times higher than that of the slower relaxing Li^+ ions at lower frequencies. The position of maximum frequency, f_{max}, of the faster relaxation was shifted to lower frequencies for the composite electrolytes and the frequency shift was more pronounced for the 7 wt% electrolyte. This change in the conductivity mechanism can be attributed to an interfacial conduction of the Li^+ ions through the Al-LLZO/PEO interface. The adsorption of the PEO on the Al-LLZO surface is expected to slow down the dynamics of the local polymer conformations and therefore the associated interfacial conduction process. However, this retardation in the dynamics is compensated by the increase of the mobile Li^+ ions and the formation of less tortuous conductive paths due to the planar geometry of the Al-LLZO as opposed to a more complex diffusion mechanism through the bulk PEO phase. The dielectric loss spectra of the LiFSI electrolytes are shown in Figure S3d. The dynamical behavior of the unfilled LiFSI electrolyte is notably different than that of the unfilled LiTFSI. A single broad relaxation is present indicating a more uniform conductivity mechanism compared to the double relaxation process in the LiTFSI electrolyte. This dynamical behavior correlates well with the more pronounced ionic cluster formation and the suggested conduction mechanism through percolating cluster domains in the LiFSI electrolytes according the SAXS and MD results that are presented below. The composite LiFSI electrolytes are characterized by a single and less broad relaxation at higher frequencies, resembling the dynamic behavior of the LiTFSI electrolytes. The impact of the electrolyte structure and the space charge on the interfacial transport in composites electrolytes is still under investigation.[22-24] Our studies showed substantially different ion dynamics (due to the different ion distribution according to SAXS and MD results) in the pristine LiTFSI and LiFSI electrolytes. However, the composite electrolytes are characterized by more uniform ion dynamics that can be corelated with the ion transport through the ceramic fillers.

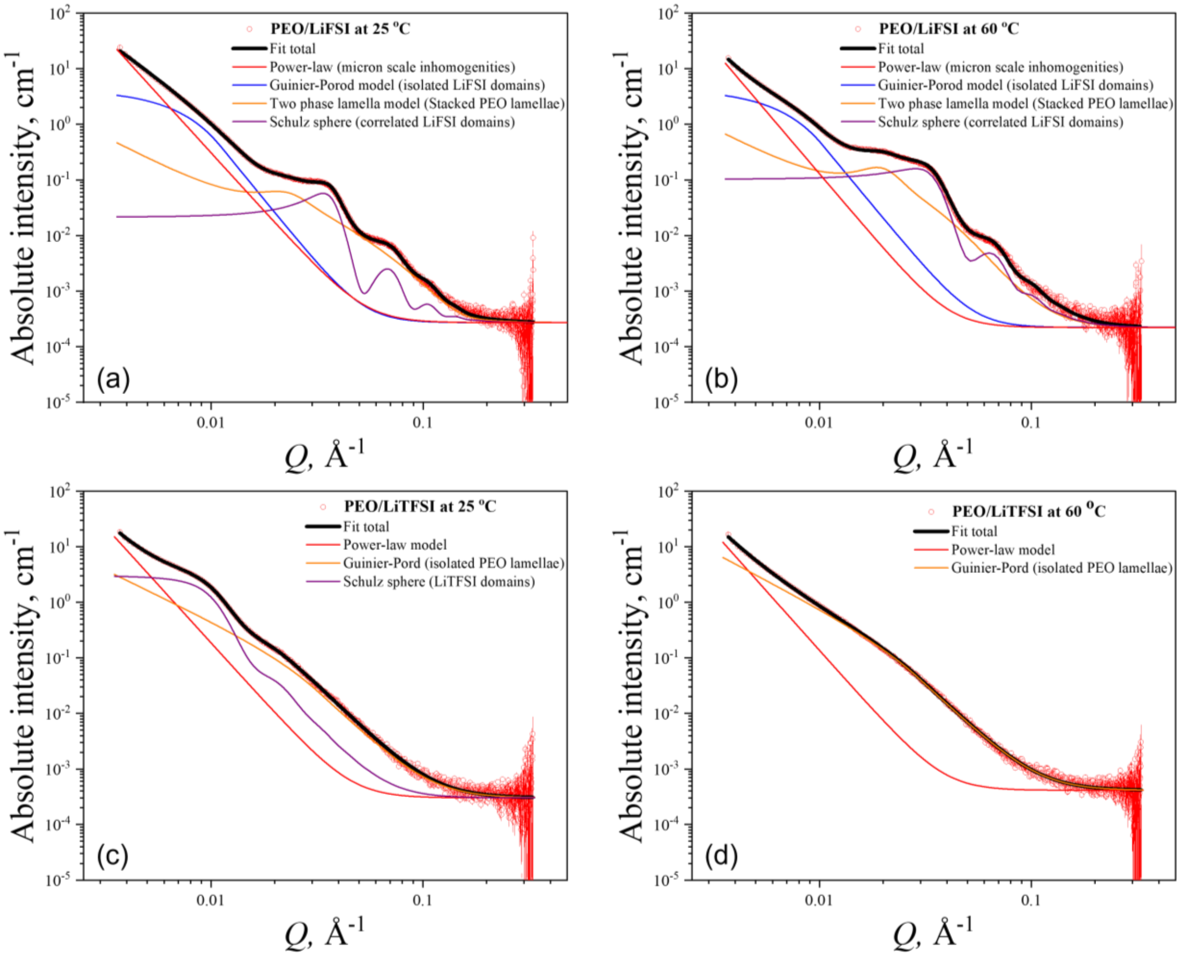

Figure 4. Experimental SAXS patterns and model-fits of the (a, b) PEO/LiFSI electrolytes at 25 ºC and 60 ºC. (c, d) PEO/LiTFSI electrolytes at 25 ºC and 60 ºC. The SAXS model-fits were based on multiple SAXS model functions as indicated in each plot. The fitting parameters of the SAXS functions that were used to fit the scattering curves are summarized in the Supporting Information.

To correlate the dynamical properties with the phase behaviors of the PEO/salts, SAXS measurements were carried out. The SAXS analysis method is described in the Experimental section. The SAXS curves of PEO/LiFSI and PEO/LiTFSI electrolytes measured at 25 ºC and 60 ºC are shown in Figure 4. It is first observed that the measured SAXS curves of PEO/LiFSI exhibit complex multiple scattering features originating from the nanoscale, multiphasic morphologies of the PEO/LiFSI electrolytes. Here, scattering vector, $Q = 4\pi \cdot sin\theta/\lambda$ with θ and λ being the half of scattering angle and X-ray beam wavelength, respectively. To identify the observed multiple scattering features, the SAXS curves of pristine PEO were also collected at the same temperatures and coplotted with those of PEO/LiFSI in Figure S4 (a) and S4 (b), respectively, for comparison purpose. At both 25 °C and 60 °C, the pristine PEO exhibited first order and second order peak maxima (red arrows). The first and second order SAXS peaks are the signature of the periodic layer-by-layer arrangements of alternating crystalline lamellae and amorphous layers stacked on top of each other within spherulites, which is the unique crystallization habit of long covalently bonded polymer chains. The lamellar long periods, $L_P's$ obtained from the first order peak position, Q_{lam}^{1st} by $L_P = 2\pi/Q_{lam}^{1st}$ were ~30.2 and ~36.0 nm, at 25 ºC and 60 ºC, respectively, and listed in Table S2. Here, the Q position of second order peak, $Q_{lam}^{2nd} = 2 \times Q_{lam}^{1st}$. The presence of first order and second order peak at 60 °C implied that the temperature is still below the melting point of PEO lamellar crystals. Also, comparing the SAXS patterns of pristine PEO to those of PEO/LiFSI presented that the scattering humps of PEO/LiFSI (scattering shoulders marked by black arrows) observed at Q_{lam}^{1st}=0.029 Å^{-1} (25 °C) and Q_{lam}^{1st}=0.023 Å^{-1} (60 °C) resembled the first order lamellar peaks of pristine PEO (red arrows) (see the dotted rectangles in both Figures S4 (a) and S4(b)). Hence, we assigned the humps as the first order peak of PEO lamellar stacks in PEO/LiFSI, while the well-developed first order (Q_{LiFSI}^{1st}) and second order (Q_{LiFSI}^{2nd}) peaks are associated with the correlated spherical LiFSI clusters (green arrows). Including the power-law scattering at Q < 0.005 Å^{-1} (orange arrows) and Guinier-type scattering shoulders near Q < 0.009 Å^{-1} (blue arrows), we combined total four SAXS models (I_{total}) to fit the measured SAXS curves as seen in Figure 4 (a) and 4(b), *i.e.*, power-law model (I_{PL}), Guinier-Porod model (I_{GP}), two-phase lamella model (I_{lamella})

and Schultz sphere model with structure factor (I_{sphere}) and, $I_{total} = I_{PL} + I_{GP} + I_{lamella} + I_{sphere}$. I_{PL} can be associated with the micrometer size scale inhomogeneities associated with such as spherulites and/or the micron scale phase separation. I_{GP} is to account for scattering shoulder observed at $Q \sim 0.009$ Å^{-1}. Since the scattering shoulders were not observed in the pristine PEO, they could be due to the added LiFSI. Two phase lamellar model is to represent the periodic stacking of alternating PEO lamellar crystal/amorphous layer and the Schultz sphere model with structure factor to comprise the correlated spherical LiFSI clusters. Additional information on the SAXS fit functions and the summarized fit parameters are provided in the SAXS models section, Equations (6) ~ (20) and Table S3. At 25 °C and 60 °C, the mean radii of the LiFSI clusters in the PEO/LiFSI electrolyte obtained from Schultz sphere model were ~8.5 and ~8.7 nm and the local volume fractions were ~0.35 and ~0.28, respectively. The reduced volume fraction of LiFSI clusters at the elevated temperature, 60 °C implies that some fraction of LiFSI clusters were solvated and diffused into the amorphous PEO phase. For the scattering shoulders appeared at $Q \sim 0.009$ Å^{-1} at both 25 °C and 60 °C, presumably LiFSI phase domains or aggregates of LiFSI clusters were formed. Note that the scattering shoulders were not observed in the pristine PEO. The applied Guinier-Porod model (I_{GP}) to fit the scattering shoulders implied that the radii of gyration, $R_g = \sim 24.0$ nm and ~ 25.6 nm at 25 °C and 60 °C, respectively. Increasing temperature from 25°C to 60°C, reduced the scattered intensity (I_{GP}) from ~45.9 cm^{-1} to ~42.7 cm^{-1}. About 7 % decrease in the scattered intensity (I_{GP}) may represent that a fraction of LiFSI domains were solvated while a larger fraction Li^+ diffused into the clustered, amorphous PEO phase. The diffusion of a larger percentage of LiFSI into amorphous phase PEO at the elevated temperature is expected as 60 °C is above the glass transition temperature of PEO and close to the melting temperature of PEO.

Therefore, amorphous PEO chains are in swollen by thermal expansion and provide more room (free volume) for the Li^+ to diffuse into the softened, amorphous PEO phase.

The SAXS patterns of PEO/LiTFSI appeared differently from those of PEO/LiFSI as seen in Figure 4(c) and 4 (d), and Figure S5. The SAXS curve of PEO/LiTFSI measured at 25 °C shows low-Q upturn at $Q < 0.005$ Å^{-1} as well as the first order and second order peak maxima. At 60 °C, the first and second peaks disappeared completely while leaving the low-Q upturn at $Q < 0.005$ Å^{-1} and broad scattering shoulder at $0.009 < Q < 0.08$ Å^{-1}. Since 60 °C is below melting point of PEO lamellar crystal, the first and second peaks seen at 25 °C and disappeared at 60°C were not due to the PEO lamellar crystals. Instead, the ordered peaks are associated with the LiTFSI clusters correlated one to another in PEO matrix. To account for the SAXS curve measured at 25 °C exhibiting the low-Q upturn, first and second order peak maxima, and broad scattering shoulder, we combined the Power-law model (I_{PL}), Schultz sphere model with structure factor (I_{sphere}) and Guinier-Porod model (I_{GP}) leading to $I_{\mathrm{total}} = I_{\mathrm{PL}} + I_{\mathrm{sphere}} + I_{\mathrm{GP}}$. To fit the SAXS curves measured at 60 °C, we used $I_{\mathrm{total}} = I_{\mathrm{PL}} + I_{\mathrm{GP}}$. From the SAXS model fit, at 25 °C, the obtained mean radius of LiTFSI from (I_{sphere}) was ~26.2 nm and the volume fraction was 0.16, Table S4. As compared to LiFSI with the mean radius, ~8.5 nm and volume fraction ~0.35 at 25 °C, LiTFSI showed about three times larger cluster (correlated clusters) size while the volume fraction was about two times less. The lower volume fraction of LiTFSI than LiFSI implied that LiTFSI solvated more than LiFSI did and diffused into PEO phase during sample preparation process. It can be thought that LiTFSI is more miscible with PEO than LiFSI. At 60 °C, the first order and second order peaks disappeared completely indicating that all the LiTFSI solvated completely in PEO matrix. Here, the miscibility difference between PEO/LiFSI and PEO/LiTFSI bears important implication in the crystallization of PEO. In immiscible polymer/filler blends, the existence of fillers in polymer matrix does not affect the crystallization of polymer significantly. This is because, the blending components are well phase separated and polymer chains can crystallize in its isolated phases without interference from the filler. In immiscible polymer/filler blends, the existence of fillers in polymer matrix does not affect the crystallization of polymer significantly. This is because, the blending components are well phase separated and polymer chains can crystallize in its isolated phases as they do in homopolymer system. In homopolymer system, polymeric chains crystallize into spherulites, where stacked crystalline lamellae radially grow outwards as bundles from the central nuclei forming spherulites.[38] The growth of lamellar crystal is facilitated by the diffusion of polymer chains onto a crystal growth front in a series followed by the crystallization of the diffused polymer chains on the crystal growth front one after another. In miscible blends, however, the diffusion of polymer chains is hampered greatly by the presence of filler.[39] In this case, the growth of lamellar crystals is frustrated, or small number of polymer chains crystallize locally into small crystals and independently into isolated crystallites rather than crystallizing into spherulites.

In miscible blends, however, the crystallization of polymer chains is hampered greatly by the filler due to the crystal growth facilitated by the diffusion of polymer chains onto other. In this case, polymer crystallization is frustrated, or polymer chains crystallize locally and independently into isolated (uncorrelated) crystallites rather than following the typical crystallization habits, *i.e.*, crystallizing into regularly stacked lamellar bundles. Hence, the missed first order SAXS peak of PEO in PEO/LiTFSI can be due to the good miscibility between PEO and LiTFSI resulting in isolated crystal growth showing no correlation peak. Based on this understanding, we assigned the broad scattering shoulder appeared at $0.009 < Q < 0.08$ Å^{-1} to isolated PEO crystals, where the applied Guinier-Porod model provide the $R_g's$ of the isolated PEO crystallites. The $R_g's$ at 25 °C and 60 °C were 3.1 and 3.4 nm, respectively.

Figure S6(a) and S6(b) compares the SAXS curves of PEO/LiTFSI and PEO/LiTFSI/LLZO. The SAXS curves of PEO/LiTFSI/LLZO were multiplied by 1.07 (~1/0.93) to normalize the scattering intensity for the less fraction of PEO/LiTFSI due to the added 0.07 (7%) LLZO. The much stronger low-Q scattering of PEO/LiTFSI/LLZO as compared to PEO/LiTFSI at 25 °C and 60 °C (red arrows), were due to the added micrometer size scale LLZO of which size is out of measurable SAXS range. The well overlapped scattering curves of PEO/LiTFSI and PEO/LiTFSI/LLZO at Q > 0.009 (25 °C) and Q > 0.015 (60 °C), on the other hand, implied that the addition of LLZO does not alter the structure of PEO and LiTFSI in the PEO/LiTFSI/LLZO. As tabulated in Table S5, the mean radius of LiTFSI cluster in the PEO/LiTFSI/LLZO at 25 °C was ~2.6 nm identical to that in in the PEO/LiTFSI. Also, the $R_g's$ of the isolated PEO crystallites at 25 °C and 60 °C were ~3.1 and ~3.3 nm, respectively. Since the $R_g's$ of PEO crystallites in the PEO/LiTFSI without LLZO at 25 °C and 60 °C were ~3.1 and ~3.2 nm, respectively, they were in the same ranges implying no impact of LLZO in the PEO/LiTFSI behavior in the PEO/LiTFSI/LLZO.

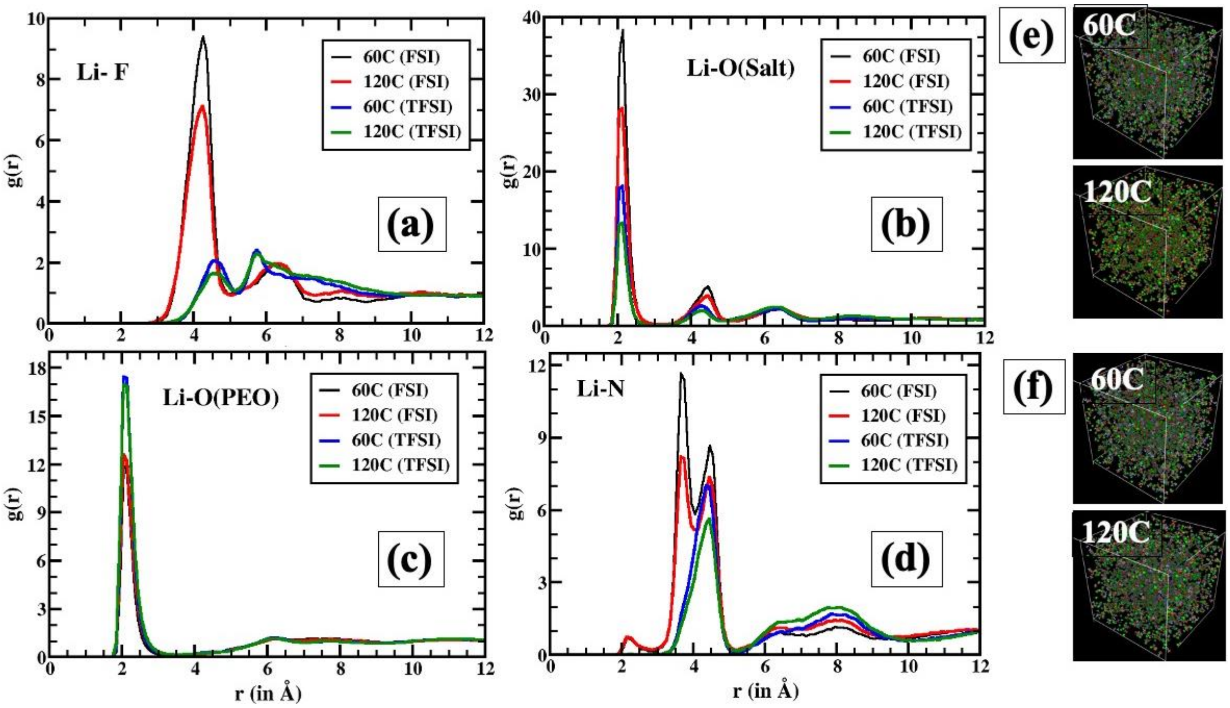

Figure 5. Structural behavior of Li^+ ions. Radial distribution function (RDF) of Li^+ with respect to (a) fluorine, (b-c) oxygen of salt and oxygen of PEO at two different temperatures, 60 ºC and 120 ºC. (d) Li^+ with nitrogen atoms of salt. (e) and (f) snapshots showing LiFSI and LiTFSI respectively. For clarity only Li^+ and Li^+ salts are shown.

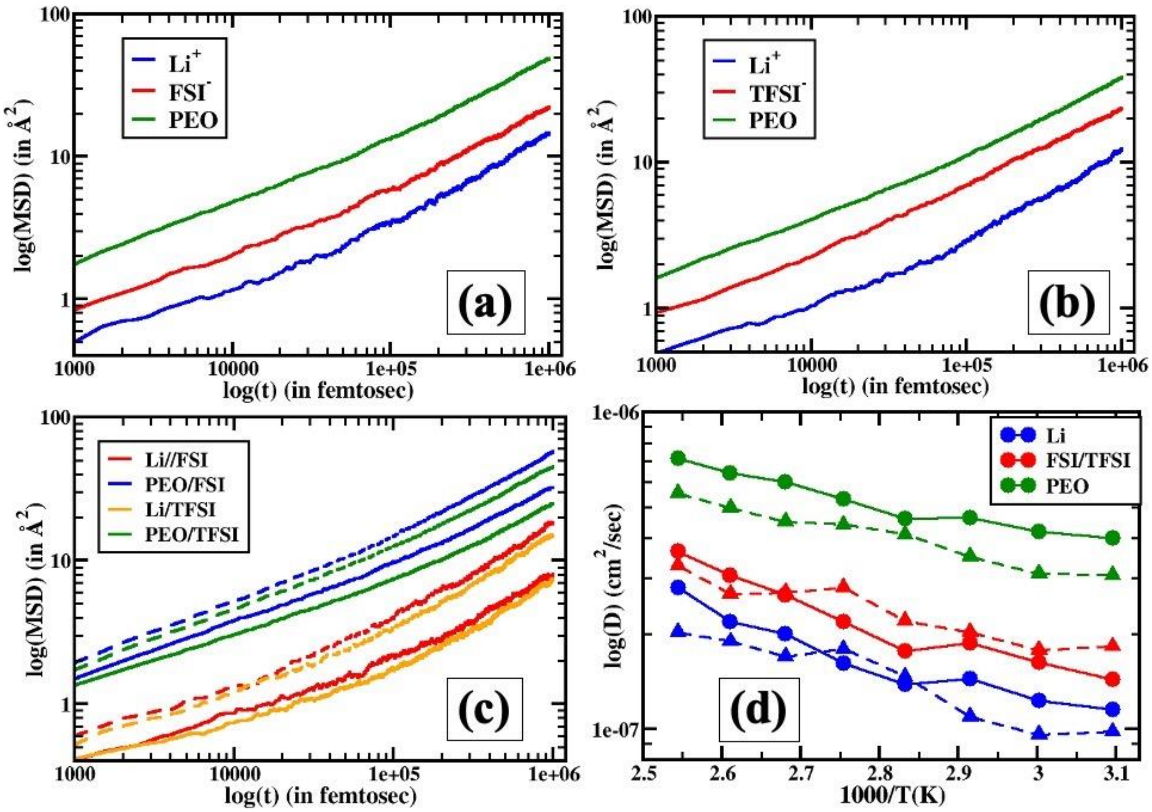

Figure 6. The mean-square-displacement (MSD) and diffusivities of the Li^+, FSI/TFSI anions, and PEO chains. (a) Comparison of Li^+, FSI and PEO MSDs for LiFSI samples at 50 ºC. (b) Comparisons of Li^+, TFSI and PEO MSDs for LiTFSI sample at 50 ºC. (c) Comparison of Li^+ and PEO dynamics (MSDs) for LiFSI and LiTFSI at 50 ºC (solid lines) and 120 ºC (dashed lines) respectively. The color schemes are shown in legends. (d) Diffusivity, calculated from Einstein's relation, of Li^+, FSI/TFSI and PEO chain. The circles (solid lines) and triangles (dashed lines) represent LiFSI and LiTFSI samples respectively.

To this end, we performed large-scale MD simulations of two systems, LiTFSI and LiFSI. The purpose of the MD simulation study to explain the structure and dynamics of individual molecules and Li^+ ions, length and time-scales that are generally unreachable in experiments.[40] Radial distribution functions (RDF) showing atomistic length-scale structures at 60 ºC and 120 ºC are shown in Figure 5. For Li^+ positions with respect to the fluorine (F), oxygen (O), and nitrogen (N) (Figures 5a, b and d) of the anions (FSI/TFSI) shows higher first peaks in FSI sample (black and red) than TFSI (blue and green). The first peak positions in these plots corresponds to Li-F, Li-O and Li-N distances respectively in salt clusters. The higher peak heights in LiFSI exhibits more agglomeration with salt than in LiTFSI. These represent formation of clustered doublet structures in LiFSI than LiTFSI. LiTFSI form smaller doublet structures. At higher temperatures, the agglomeration becomes weaker, exhibited by shorter RDF peaks representing availability of more free Li^+ ions. While the FSI clusters are more pronounced with the Li^+ salt, LiTFSI clusters around oxygen of PEO (blue and green lines in Figure 5c) show higher agglomeration than LiFSI (black and red). These RDFs represent that structurally the Li^+ preferably clusters with FSI domain in LiFSI, and smear into PEO chains in LiTFSI as observed in SAXS (Figure 4). There are certainly large number of Li^+ from LiFSI remains within the free state in FSI for transport. The most distinctive structure is observed in Li^+ and nitrogen (N) of Li^+ salt (Figure 5d). The nitrogen is the negatively charged atom in the LiFSI/LiTFSI (Figure S10). For LiTFSI sample, the first peak (~4.35 Å) followed by a broad second peak at longer distances, representing Li^+ salt form weak agglomeration (slower relaxation in DSC) but self-assembled in a percolated amorphous spread over longer length-scales as the Li^+ in LiTFSI are closely packed with PEO domains (faster relaxation).[41,42] However, for LiFSI samples, an extremely weak first peak (2.15 Å) followed by a second shell layered peaks as exhibited by second and third peaks represents a layered agglomerated structure of Li^+ with FSI. The larger amorphous broad peak can also be seen because of the dispersed Li^+ distribution over the entire simulation box. For both the cases, increase in temperature reduces the peak heights resulting in weaker agglomeration as observed in SAXS. The snapshots of the Li^+ salt domains for these two systems are shown in Figure 5e and f. Higher resolution snapshots are available in the SI (Figure S11 and S12). The dynamics of the different species are obtained from MD simulations, represented by the mean-square-displacement (MSD), $MSD = \frac{1}{N}\sum_{i=1}^{N}|r_i(t) - r_i(0)|^2$ (where N is the total number atoms, $r_i(t)$ and $r_i(0)$ are the positions of atoms at time t and zero) and diffusion coefficient (D) as shown in Figure 6. The MSDs, representing the motion of the atoms/molecules over time, at 50 ºC for Li^+(blue), anions FSI/TFSI and the PEO chains (green) are shown in Figure 6a and 6b. The PEO monomeric motions (green) are the fastest due to a large number of monomers in a PEO polymer chains that provides higher degree of flexibility and hence movement. Moreover, the PEO chain motion is governed by the reptation dynamics which is segmental. The PEO monomers also have their own dynamics, and a PEO chain center-of-mass dynamics. Therefore, the PEO has larger diffusivity due to the fact that the majority of the PEO chain monomers are free from clusters and can move due to their flexibility even though some monomers are part of the cluster. The FSI/TFSI (blue) shows the intermediate motion, while the Li^+ shows the slowest MSD due to their agglomerated states within a cluster in LiFSI and percolated states in LiTFSI. Interestingly MSDs of Li^+, TFSI and PEO (Figure 6b) follow each other parallelly at longer times, meaning they show coupled dynamics. However, in LiFSI system the Li^+ MSD increases in longer times that approaches FSI representing the clustering of Li^+ with FSI and decoupled dynamics of Li^+. In Figure 6c, the MSDs of Li^+ and PEO are compared for LiFSI and LiTFSI systems at 50 ºC and 120 ºC. For both the temperatures, Li^+ dynamics (red and blue) are faster in LiFSI than LiTFSI (green and orange). MSD for Li^+ at all temperatures are shown in Figure S13. As temperature increases from 50 ºC (solid lines) to 120 ºC (dashed line) the motion becomes faster due to entropic effect. The diffusivity (D), calculated from the Einstein's relation, $D = \frac{1}{6}\lim_{t\to\infty}\frac{<|x_i(t)-x_i(0)|^2>}{\Delta t}$, are shown in Figure 6d.[43] The diffusion coefficients match exactly with previously reported diffusion coefficients by Choo et al.[27] The fastest diffusivity is seen in PEO (green) as the segmental motion[27] of polymer chain in a polymer-Li^+ salt composite is the fastest. The FSI/TFSI are intermediate anionic self-diffusion and the Li^+ diffusivity exhibit slow movement because of agglomeration within the domains. The LiTFSI (triangles) show slowest movement. The diffusivities of Li^+ and FSI (blue and red spheres) of LiFSI are closer to each other compared to Li^+ and TFSI of LiTFSI (red and blue triangles) representing more agglomerated Li^+/FSI clusters conforming with our structural findings in SAXS (Figure 4) and RDF observations (Figure 5). To address the ability of Li^+ releasing from the cluster to hop to another cluster, the dissociation energies of Li^+ ions are calculated using atomistic MD simulations. The total energies as a function of time, obtained from MD simulations, for LiFSI and LiTFSI systems are observed to be 50,000eV and 200,000eV as shown in SI Figure S14. The higher total energy in LiTFSI system compared to LiFSI system correspond to large dissociation energy requirement to break free Li^+ ions from the clustered phase. Likewise, a lower dissociation energy is needed for Li^+ to hop from cluster to cluster in LiFSI system. This explains why Li^+ exhibits higher diffusivity (Figure 5) and conductivity (Figure 2) in LiFSI system compared to LiTFSI system.

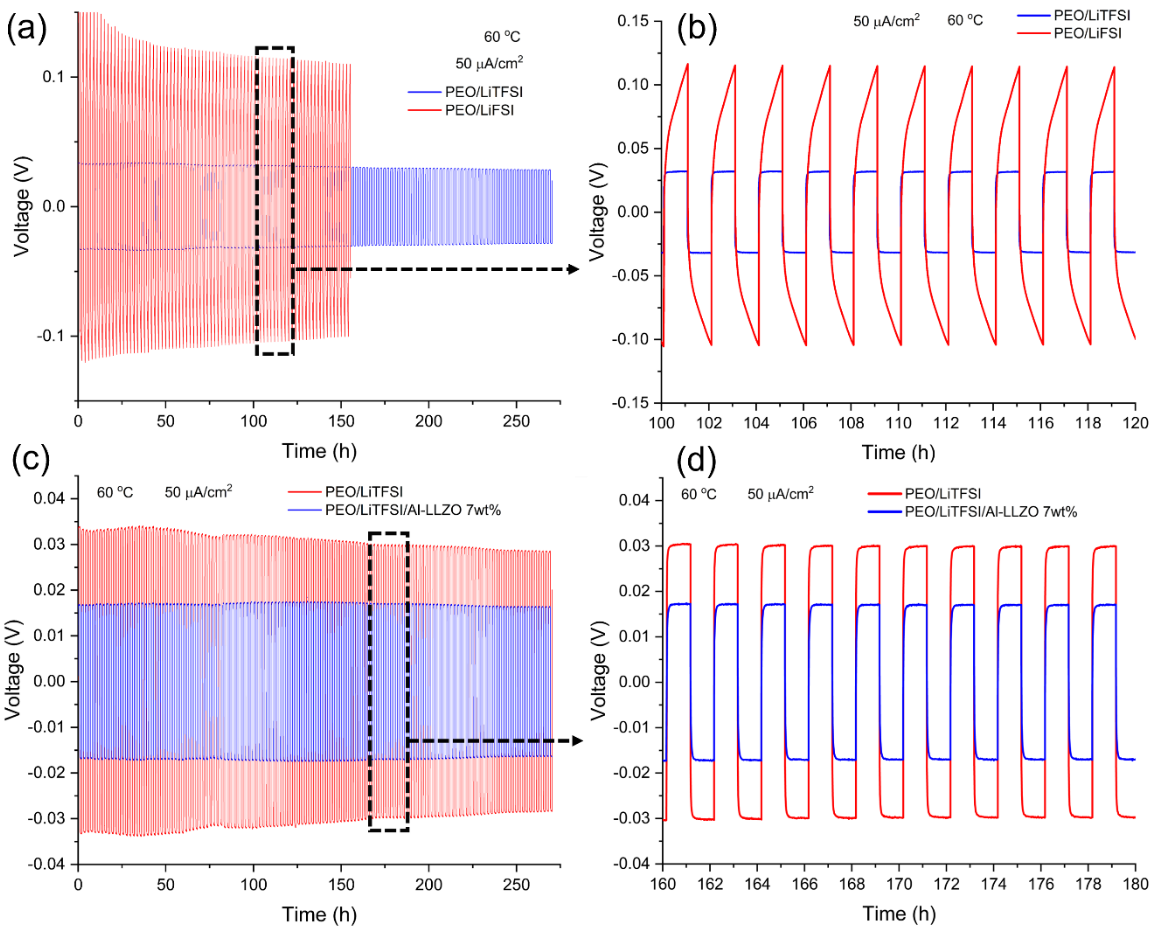

Figure 7. Comparison of the long term galvanostatic cycling of the (a, b) LiFSI and LiTFSI electrolytes and (c, d) LiTFSI and LiTFSI composite filled with 7 wt% Al-LLZO at 60 °C and 50 μA/ cm^{-2}.

Striping/plating experiments were performed to compare the electrochemical stability of the electrolytes. Comparison plots of the long-term galvanostatic cycling at 60 °C and 50 μA cm^{-2} current density for the PEO/LiFSI, PEO/LiTFSI, and PEO/LiTFSI/Al-LLZO 7wt% are shown in Figure 7. Although the LiFSI electrolytes are more conductive compared to the LiTFSI electrolytes (Figure 2), the overpotential values in Figure 7a and b show the opposite dependence. The PEO/LiTFSI overpotential values are less than half compared to those of the PEO/LiFSI. This behavior can be associated with the formation of the solid electrolyte interface (SEI) due to the electrolyte/salt degradation during the galvanostatic cycling. As can be seen from Figure S15 the initial surfaces of the PEO/LiFSI, PEO/LiFSI/Al-LLZO 7wt%, PEO/LiTFSI, and PEO/LiTFSI/Al-LLZO 7wt% differ. More specifically, the PEO chemical composition derived from the C1s spectra (Figure S15a) shows that the PEO/LiFSI and PEO/LiFSI/Al-LLZO have C-Li bonds. The salt composition derived from the Li1s spectra (Figure S15b) are similar for the LiTFSI and LiFSI based samples with only the PEO/LiTFSI/Al-LLZO causing an increased lithium carbonate content on the surface. These initial different chemical states may result in the formation of different SEIs or may thermally degrade differently. Impedance measurements during galvanostatic striping/plating provide information on the interfacial electrolyte-Li metal resistance and its variation during the EIS formation. Impedance measurements were performed after 70 striping/plating cycles at 60 ºC with a 50 μA cm^{-2} current density. The spectra are summarized in Figure S18 in the Supporting Information. The interfacial resistance was higher for the PEO/LiFSI electrolyte (~370 Ohm) and was found to decrease systematically for the PEO/LiTFSI (~294 Ohm) and the PEO/LiTFSI/Al-LLZO 7 wt% (~87 Ohm). The investigation of the SEI formation and the decomposition of the electrolytes is ongoing. The voltage time measurements showed the formation of polarization peaks (Figure 7b) for the PEO/LiFSI electrolyte. Such polarization effects relate to gradients in the local electric field due to heterogeneities in the distribution of charge carriers in the bulk structure of the electrolyte. Such heterogeneities and concentration gradients were evident in the SAXS measurements (Figure 4) and MD simulation (Figure 5) studies. The LiFSI molecules were found to be more susceptible to the formation of cluster domains whereas, the LiTFSI showed a better miscibility (solvation) and dispersion in the PEO matrix. The Al-LLZO platelets further improved the electrochemical stability of the PEO/LiTFSI electrolyte and an additional decrease of the overpotential values was observed compared to the PEO/LiTFSI electrolyte (Figure 7c, d). These results are in good agreement with the additional electrochemical measurements in Figures S7 – 9. The critical current densities of the pristine and composite LiFSI electrolytes are significantly lower than those of the respective LiTFSI electrolytes and the long-term cycling of the LiFSI composite electrolyte failed much sooner than the LiTFSI composite electrolyte indicating a poor resistance to the dendrite formation. The synergistic effects between multi-length scale properties such as the good solvation properties of the LiTFSI in the nanoscale, and the altered conductivity mechanism due to the incorporation of micrometer sized Al-LLZO platelets can be utilized toward tailoring the macroscopic electrochemical properties of composite electrolytes against a Li metal anode.

CONCLUSION

The nanoscale Li^+ ion transport in ceramic-polymer composite electrolytes was correlated with the polymer segmental dynamics, the nanoscale structure and functionality and the macroscopic electrochemical stability of the electrolyte. PEO filled with LiTFSI or LiFSI salts was used as the polymer matrix and a garnet electrolyte Al-LLZO with planar geometry was used for the ceramic phase. The dissociation of the Li^+ ion conduction mechanism from the slow polymer segmental dynamics was synergistically enhanced through ion-hopping mechanism that was facilitated tangentially along the surface of the Al-LLZO platelets and by controlling the size of the ionic cluster domains. The ion transport was described by a bimodal distribution of relaxation processes attributed to the less mobile Li^+ ions that are strongly bound to the PEO and to the more mobile dispersed Li^+ ions. An increased ratio between the number density of the more mobile and the less mobile ions was evident in the more conductive composite electrolytes compared to the pristine electrolyte due to the interfacial conduction of the Li^+ ions through the less tortuous Al-

LLZO/PEO interface. The chemical structure of the Li^+ salt was correlated with the size of the ionic cluster domains. Analysis of the SAXS patterns for the LiTFSI and LiFSI electrolytes showed about three times larger cluster size for the LiTFSI while the volume fraction was about two times less. The lower volume fraction of LiTFSI than LiFSI implied that LiTFSI solvated more than LiFSI did and diffused into the PEO phase indicating that it is percolated within the PEO phase compared to LiFSI. The experimental results are corroborated with MD simulations that exhibited the diffusivities of Li^+ and FSI of LiFSI are closer to each other compared to Li^+ and TFSI of LiTFSI representing more agglomerated Li^+/FSI clusters with doublet structure as confirmed by RDF and SAXS. The calculated dissociation energies of Li^+ ions as a function of time for LiFSI and LiTFSI showed that the lower dissociation energy for Li^+ helps these ions hop from cluster to cluster in LiFSI system, while the four times higher dissociation energies tightly bind the Li^+ ions within the cluster in LiTFSI system. Therefore, it is evident that Li^+ would exhibit higher diffusivity and conductivity in LiFSI system compared to LiTFSI system. Although the LiFSI electrolytes are more conductive, they were found to be more susceptible to the formation of cluster domains whereas the LiTFSI showed a better percolated structures with PEO matrix. The better Li^+ ion solvation in nanoscale domains and the incorporation of Al-LLZO platelets resulted in improved critical current densities and long-term cycling of the LiTFSI electrolytes.

EXPERIMENTAL

Sample Preparation and Electrochemical Measurements. Electrospinning techniques were used for the synthesis of the Al-LLZO platelets. The precursor solutions and the experimental setup are summarized in our previous studies.[44] Electrolytes were prepared by dissolving lithium bis(trifluoromethanesulfonyl)imide (LiTFSI, Sigma Aldrich) or lithium bis(fluorosulfonyl) imide (LiFSI, Sigma Aldrich) and polyethylene oxide (PEO, MW 400,000, Sigma Aldrich) (ethylene oxide to Li molar ratio, EO:Li = 19.6:1) in acetonitrile (ACN). The solution was stirred overnight before it was cast onto Teflon plates. Composite electrolytes with 7 and 15 wt% in Al-LLZO were prepared by adding proportionate amounts of Al-LLZO in the PEO/salt/ACN solution and stirring until most of the solvent was evaporated. The thick Al-LLZO suspension was cast onto Teflon plates. The retrieved electrolytes (approximately 60 mm thick) were dried in vacuum overnight at 80 °C. Striping/plating experiments at several current densities and long term galvanostatic cycling were performed on a Biologic VSP potentiostat at 60 °C. Coin cells were assembled using Li metal discs for the electrodes. Broadband dielectric relaxation spectroscopy (DRS) measurements were carried out on a Novocontrol Alpha analyzer connected to a Quatro Cryosystem for regulating the temperature (temperature stability: 0.1 ^{O}C). Measurements were performed isothermally in broad frequency (10^{-2} to 10^{7} Hz) and temperature (120 to -30 °C) ranges. A Zeiss Merlin VP SEM/STEM was used for the scanning electron microscopy (SEM) imaging.

Typical Characterizations. Small-angle X-ray scattering (SAXS) measurements were carried out on a Xenocs Xeuss 3.0 instrument equipped with D2+ MetalJet X-ray source (Ga K_{α}, λ = 1.3414 Å). The samples in were aligned perpendicular to the direction of the X-ray beam (transmission mode) and the scattered beam was recorded on a Dectris Eiger 2R 4M hybrid photon counting detector with a pixel dimension of 75 × 75 μm^2. The collected 2-dimensional (2D) SAXS images were circularly averaged and expressed as intensity versus Q, where $Q = (4\pi \sin \theta)/\lambda$ after subtraction of background scattering. The sample-to-detector distance was 1800 mm and the exposure time was 600 s. An ESCALAB Xi+ (Thermo Fisher Scientific) spectrometer fitted with a monochromatic Al Kα source and operating at a power of 200 W was used to obtain the X-ray Photoelectron Spectroscopy data. The samples were introduced into the ultra-high vacuum (10^{-10} mbar) chamber of the instrument. The survey spectra were recorded with a pass energy of 150 eV and the high-resolution spectra with 20 eV. All spectra were corrected for charging, where necessary, with regards to the C-C peak with a binding energy of 284.8 eV. In molecular dynamics simulations, atomistic MD simulations were carried out using LAMMPS MD package[45] on Summit supercomputer. The PEO molecules were generated with 12 repeat units of ethylene oxide (EO) monomers for computational efficiency. There are fractional charges on the PEO backbone atoms. The TFSI and FSI each contain -1 charges precisely placed at nitrogen atom site, and the Li ions are point particles with +1 charges. The polymer and LiTFSI/LiFSI molecular architectures are shown in the top panel of SI Figure (S1). Two different systems, PEO/FSI/Li as System I, PEO/TFSI/Li as System II were build using Moltemplate package.[46]

Force field parameters. The interactions for the different atoms in the molecular dynamics (MD) simulation are governed by force-field (FF) parameters that are based on DFT calculations and are readily available from various database and published literature. For PEO, we used GROMOS-54a FF,[47] a common FF use in polymers and biopolymers. This FF is particularly optimized for long-chain alkanes and polyether compounds. The FF consists of Lennard-Jones (LJ) interactions and Coulombic interactions for charged atoms. For the Li^+ salt, optimized potential for simulation all atom (OPLS-AA) force-field[48,49] was used. The cross interactions are modelled with LJ and Coulomb potentials for charged atoms.[50]

Initial System Setup. A single PEO molecule was built with Moltemplate and an energy minimization on the single PEO molecule were performed. The single PEO chain was replicated to build a 3 PEO system. The FSI/TFSI and Li^+ are added for the two different systems. The whole system is then replicated to build a large box of ~$26 \times 22 \times 23$ nm^3. This low-density box of PEO and FSI/TFSI with Li ions are then compressed to build high density composites. For System I the system size was $13.6 \times 13.6 \times 13.6$ nm^3 at a density 1.26 g cm^{-3}, and for System II the system size was 14.7×14.7×14.7 nm^3 box at a density of 1.3 g cm^{-3}. Finally, these two initial systems were equilibrated for 3 nanoseconds before doing the production runs.

Permittivity Data Analysis. The permittivity data were fitted using two HN expressions and a power law contribution,

$$\varepsilon * (\omega) = \varepsilon_\infty + \sum_{i=1}^{2} \frac{\Delta\varepsilon_i}{\left[1+\left(i\omega\tau_{0,i}\right)^{1-\alpha_i}\right]^{\beta_i}} - i\frac{\sigma_0}{\varepsilon_0}\omega^{-s} \tag{2}$$

The imaginary part of the complex permittivity function can be expressed as,

$$\varepsilon''(\omega) = \sum_{i=1}^{2} \Delta\varepsilon_i \frac{\sin(\beta_i\phi_i)}{\left[1+2(\omega\tau_{0,i})^{1-\alpha_i}\sin(\frac{1}{2}\alpha_i\pi)+(\omega\tau_{0,i})^{2(1-\alpha_i)}\right]^{\beta_i/2}} + i\frac{\sigma_0}{\varepsilon_0}\omega^{-s} \tag{3}$$

where,

$$\varphi_i = arctan[\frac{(\omega\tau_{o,i})^{1-\alpha}cos(\alpha_i\pi/2)}{1+(\omega\tau_{o,i})^{1-\alpha}sin(\alpha_i\pi/2)}] \tag{4}$$

In Eqs. 2 and 3, $\omega = 2\pi f$ is the angular frequency, the power law exponent $s \leq 1$ defines the slope of the conductivity contribution (s = 1 for dc conductivity), the dielectric relaxation strength is defined as $\Delta\varepsilon = \varepsilon_s - \varepsilon_\infty = \frac{2}{\pi}\int_0^\infty \varepsilon''(\omega) d\,ln\,\omega$ where ε_s and ε_∞ are the low (static) and high frequency values of the real part of permittivity, respectively. ε_0 is the vacuum permittivity, the slopes (or broadening) of the peak at high and low frequencies is associated with the shape parameters a, b $(0 < (1-\alpha)\beta \leq 1,$ and $0 \leq \alpha < 1)$. The characteristic time $\tau_0 = 1/2\pi f_o$ is associated to the maximum frequency, f_{max}, of the relaxation process,

$$f_{max,i} = f_{o,i}[\frac{sin[(1-a_i)\pi/(2+2\beta_i)]}{sin[(1-a_i)\beta_i\pi/(2+2\beta_i)]}]^{1/(1-\alpha_i)} \tag{5}$$

SAXS data analysis. The two-phase lamellar model to account for the semicrystalline PEO phase structure can be written as follows,[51-54]

$$I_{lamella}(Q) = \frac{2\pi}{TQ^2}|F_{lamella}(Q)|^2|Z(Q)|^2 \tag{6}$$

where, $|F_{lamella}(Q)|^2$ is the form factor of the lamella with the average lamellar thickness áTñ given by Equation (7),

$$|F_{lamella}(Q)|^2 = \frac{2(\Delta\rho)^2}{Q^2}\left[1 - \cos(QT)e^{-Q^2\sigma_T^2/2}\right] \tag{7}$$

where, σ_T is the Gaussian standard deviation of the lamellar thickness, T with polydispersity, $p_T = \sigma_T/T$. $|Z(Q)|^2$is the lattice factor for the three-dimensional lamellar stack with infinite stack height given by Equation (8),

$$Z(Q) = Re\left|\frac{1+H_L(Q)}{1-H_L(Q)}\right| \tag{8}$$

where, $Re||$ stands for real number and $H_L(Q)$ is the one-dimensional Fourier-transform of $h_L(L)$. The choice for $h_L(L)$ in this study is a shifted Gaussian,

$$h_L(L) = (2\pi\sigma_L^2)^{-1/2}exp\left[-\frac{(L-\langle L\rangle)^2}{2\sigma_L^2}\right] \tag{9}$$

where, $\langle L\rangle$ is the average distance of adjacent lamellae layers (*i.e.,* long spacing) in the stacks over the Gaussian distribution of L with polydispersity, p_L and standard deviation, σ_L , defined as $p_L = \sigma_L/L$.

The scattering from concentrated sphere with Schulz distribution can be expressed as,[55,56]

$$I_{sphere}(Q) = \left|\langle F_{sphere}(Q)\rangle\right|^2 S(Q) \tag{10}$$

where, the form factor, $\left|\langle F_{sphere}(Q)\rangle\right|^2$ is given as,

$$\left|\langle F_{sphere}(Q)\rangle\right|^2 = \left|\int_0^\infty F_{sphere}(Q)h(R)dR\right|^2 \tag{11}$$

Here, $h(R)$ is Schulz distribution of sphere radius, R[57] and $F_{sphere}(Q)$ is defined as,

$$F_{sphere}(Q) = 3V_{sphere}(\Delta\rho)\frac{\sin(QR)-QRcos(QR)}{(QR)^3} \tag{12}$$

In Equation (10), the structure factor, $S(Q)$ is written as,

$$S(Q) = \frac{1}{1+24\eta_{HS}G(2QR)/2QR} \tag{13}$$

where, $G(x)$ is,

$$G(x) = \alpha\frac{\sin(x)-xcos(x)}{x^2} + \beta\frac{2xsin(x)+(2-x^2)\cos(x-2)}{x^3} +$$

$$\gamma\frac{-x^4\cos(x)+4[(3x^2-6)\cos(x)+(x^3-6x)\sin(x)+6]}{x^5} \tag{14}$$

With these definitions for α, β, γ:

$$\alpha = \frac{(1+2\eta_{HS})^2}{(1-\eta_{HS})^4};\ \beta = \frac{6\eta_{HS}(1+\eta_{HS}/2)^2}{(1-\eta_{HS})^4};\ \gamma = \frac{\eta_{HS}/2(1+2\eta_{HS})^2}{(1-\eta_{HS})^4} \tag{15}$$

The Guinier-Porod model is given by,[58]

$$I_{GP}(Q) = \frac{G_1}{Q^s}exp[\frac{-Q^2R_g^2}{3-s}]\ for\ Q \leq Q_1\ (Guinier\ term) \tag{16}$$

$$I_{GP}(Q) = \frac{D}{Q^m}\ for\ Q \geq Q_1\ (Porod\ term) \tag{17}$$

where, $I(Q)$ is the scattered intensity, Q is the scattering variable, R_g is the radius of gyration, m is the Porod exponent, s is the dimension variable, and G and D are the Guinier and Porod scale factors, respectively. For the Guinier and Porod terms to be continuous at Q_1 the following relations are derived:

$$Q_1 = R_g^{-1}\left(\frac{(m-s)}{2}\right)^{\frac{1}{2}} \tag{18}$$

$$D = G\,exp\left(\frac{-Q_1^2 R_g^2}{3-s}\right) Q_1^{(m-s)} = \frac{G_1}{R_g^{(m-s)}}\ exp\left(-\frac{m-s}{2}\right)\left(\frac{(m-s)(3-s)}{2}\right)^{(m-s)/2} \tag{19}$$

Power-law model is read as,

$$I_{PL} = f_s Q^{-m} \tag{20}$$

where, f_s is a scale factor, and m is the Porod exponent.

ASSOCIATED CONTENT

Supporting Information.

The Supporting Information is available free of charge at https://pubs.acs.org/doi/.

Tables of VFT fitting parameters, fitting analysis, dielectric loss spectra, temperature dependence of the conductivity relaxation mechanisms, SAXS data and comparison, stripping/plating measurement data, long term galvanostatic cycling data, molecular dynamics simulation initial setup and data, mean square displacement, total disassociation energies from simulation analysis, HRXPS data, SEM and SEM-EDX images, EIS data, Apparent activation energies data, and summarized Arrhenius data (PDF)

AUTHOR INFORMATION

Corresponding Authors

Georgios Polizos - Electrification and Energy Infrastructures Division, Oak Ridge National Laboratory, Oak Ridge, TN 37831, USA; Email: polyzosg@ornl.gov

Jianlin Li - Electrification and Energy Infrastructures Division, Oak Ridge National Laboratory, Oak Ridge, TN 37831, USA; Email: jianlin.li@anl.gov

Authors

Monojoy Goswami - Chemical Sciences Division, Oak Ridge National Laboratory, Oak Ridge, TN 37831, USA

Jong K. Keum - Neutron Scattering Division, Oak Ridge National Laboratory, Oak Ridge, TN 37831, USA; Center for Nanophase Materials Sciences, Oak Ridge National Laboratory, Oak Ridge, TN 37831, USA

Lilin He - Neutron Scattering Division, Oak Ridge National Laboratory, Oak Ridge, TN 37831, USA

Charl J. Jafta - Electrification and Energy Infrastructures Division, Oak Ridge National Laboratory, Oak Ridge, TN 37831, USA

Jaswinder Sharma - Electrification and Energy Infrastructures Division, Oak Ridge National Laboratory, Oak Ridge, TN 37831, USA

Yangyang Wang - Center for Nanophase Materials Sciences, Oak Ridge National Laboratory, Oak Ridge, TN 37831, USA

Logan T. Kearney - Chemical Sciences Division, Oak Ridge National Laboratory, Oak Ridge, TN 37831, USA

Runming Tao - Electrification and Energy Infrastructures Division, Oak Ridge National Laboratory, Oak Ridge, TN 37831, USA; orcid.org/0000-0002-1442-8433

Author Contributions

G. P. contributed to experimental results, data analysis, design of experiment, original manuscript writing. M. G. performed MD simulations, explained the experimental results from atomistic MD simulations and contribute to manuscript writing. J. K. K., L. K. and L. H conducted SAXS/WAXS experiment and edited the manuscript. C. J. J. did XPS work. J. S. dis some sample preparation and material synthesis. Y. W. did dielectric spectroscopy measurements. R. T. did PEO-based electrolyte preparation and stripping/plating measurements. J. L. contributed to conception, experiment design, data analysis and manuscript editing.

Notes

The authors declare no competing financial interest.

ACKNOWLEDGMENT

This research at Oak Ridge National Laboratory, managed by UT Battelle LLC, for the US Department of Energy (DOE) under contract DE-AC05-00OR22725, was sponsored by the Vehicle Technologies Office (Program Managers: Peter Faguy and Haiyan Croft). This research used the resources of the Center for Nanophase Materials Sciences (CNMS) and Spallation Neutron Source (SNS), which are DOE Office of Science User Facilities. This research used resources of the Oak Ridge Leadership Computing Facility at the Oak Ridge National Laboratory, which is supported by the Office of Science of the US Department of Energy under Contract No.

DE-AC05-00OR22725. Part of the MD simulations was performed at the National Energy Research Scientific Computing Center (NERSC), a DOE Office of Scientific User Facility supported by the DOE Office of Science under Contract DE-AC02- 05CH11231.

REFERENCES

(1) Li, J.; Fleetwood, J.; Hawley, W. B.; Kays, W. From Materials to Cell: State-of-the-Art and Prospective Technologies for Lithium-Ion Battery Electrode Processing. *Chem. Rev.* **2022**, *122*, 903−956.

(2) Fan, L. Z., He, H.; Nan, C. W. Tailoring Inorganic–Polymer Composites for the Mass Production of Solid-State Batteries. *Nat. Rev. Mater.* **2021**, *6*, 1003−1019.

(3) Manthiram, A.; Yu, X.; Wang, S. Lithium Battery Chemistries Enabled by Solid-State Electrolytes. *Nat. Rev. Mater.* **2017**, *2*, 16103.

(4) Hallinan, D. T.; Balsara, N. P. Polymer Electrolytes. *Annu. Rev. Mater. Res.* **2013**, *43*, 503−525.

(5) Eisenberg, A.; Kim, J. S. Introduction to Ionomers. **1998**, John Wiley.

(6) Zhou, G.; Li, F.; Cheng, H. M. Progress in Flexible Lithium Batteries and Future Prospects. *Energy Environ. Sci.* **2014**, *7*, 1307−1338.

(7) Hueso, K. B.; Armand, M.; Rojo, T. High Temperature Sodium Batteries: Status, Challenges and Future Trends. *Energy Environ. Sci.* **2013**, *6*, 734−749.

(8) Chen, F.; Yang, D.; Zha, W.; Zhu, B.; Zhang, Y.; Li, J.; Gu, Y.; Shen, Q.; Zhang, L.; Sadoway, D. R. Solid Polymer Electrolytes Incorporating Cubic $Li_7La_3Zr_2O_{12}$ for All-Solid-State Lithium Recharge-able Batteries. *Electrochim. Acta* **2017**, *258*, 1106−1114.

(9) Bae, J.; Li, Y.; Zhao, F.; Zhou, X.; Ding, Y.; Yu, G. Designing 3D Nanostructured Garnet Frameworks for Enhancing Ionic Conductivity and Flexibility in Composite Polymer Electrolytes for Lithium batteries. *Energy Storage Mater.* **2018**, *15*, 46−52.

(10) Zhao, Y.; Yan, J.; Cai, W.; Lai, Y.; Song, J.; Yu, J.; Ding, B. Elastic and Well-Aligned Ceramic LLZO Nanofiber Based Electrolytes for Solid-State Lithium Batteries. *Energy Stor. Mater.* **2019**, *23*, 306−313.

(11) Popovic, J.; Brandell, D.; Ohno, S.; Hatzell, K. B.; Zheng, J.; Hu, Y. Y. Polymer-Based Hybrid Battery Electrolytes: Theoretical Insights, Recent Advances and Challenges. *J. Mater. Chem. A* **2021**, *9*, 6050−6069.

(12) Liang, H. P.; Zarrabeitia, M.; Chen, Z.; Jovanovic, S.; Merz, S.; Granwehr, J.; Passerini, S.; Bresser, D. Polysiloxane-Based Single-Ion Conducting Polymer Blend Electrolyte Comprising Small-Molecule Organic Carbonates for High-Energy and High-Power Lithium-Metal Batteries. *Adv. Energy Mater.* **2022**, *12*, 2200013.

(13) Park, J.; Staiger, A.; Mecking, S.; Winey, K. I. Enhanced Li-Ion Transport through Selectively Solvated Ionic Layers of Single-Ion Conducting Multiblock Copolymers. *ACS Macro Lett.* **2022**, *11*, 1008−1013.

(14) Choi, H.; Kwon, H.; Kim, H. T. Hybrid Electrolyte of $Li_{1.3}Al_{0.3}Ti_{1.7}(PO_4)_3$ Nanofibers and Cross-linked Gel Electrolyte for Li Metal Batteries. *ACS Appl. Energy Mater.* **2023**, *6*, 802−811.

(15) Janek, J.; Zeier, W. G. Challenges in Speeding Up Solid-State Battery Development. *Nat. Energy* **2023**, *8*, 230−240.

(16) Dirican, M.; Yan, C.; Zhu, P.; Zhang, X. Composite Solid Electrolytes for All-Solid-State Lithium Batteries. *Mater. Sci. Eng. R.* **2019**, *136*, 27−46.

(17) Sethi, G. K.; Jiang, X.; Chakraborty, R.; Loo, W. S.; Villaluenga, I.; Balsara, N. P. Anomalous Self-Assembly and Ion Transport in Nanostructured Organic−Inorganic Solid Electrolytes. *ACS Macro Lett.* **2018**, *7*, 1056−1061.

(18) Shan, X.; Zhao, S.; Ma, M.; Pan, Y.; Xiao, Z.; Li, B.; Sokolov, A. P.; Tian, M.; Yang, H.; Cao, P. F. Single-Ion Conducting Polymeric Protective Interlayer for Stable Solid Lithium-Metal Batteries. *ACS Appl. Mater. Interfaces* **2022**, *14*, 56110−56119.

(19) Liang, J.; Tao, R.; Tu, J.; Guo, C.; Du, K.; Guo, R.; Zhang, W.; Liu, X.; Guo, P.; Wang, D.; Dai, S.; Sun, X. G. Design of a Multi-Functional Gel Polymer Electrolyte with a 3D Compact Stacked Polymer Micro-Sphere Matrix for High-Performance Lithium Metal Batteries. *J. Mater. Chem. A*, **2022**, *10*, 12563−12574.

(20) Cai, W.; Zhang, Y.; Li, J.; Sun, Y.; Cheng, H. Single-Ion Polymer Electrolyte Membranes Enable Lithium-Ion Batteries with a Broad Operating Temperature Range. *ChemSusChem* **2014**, *7*, 1063−1067.

(21) Du, Z.; Chen, X. C.; Sahore, R.; Wu, X.; Li, J.; Dudney, N. J. Effects of Plasticizer Content and Ceramic Addition on Electrochemical Properties of Cross-Linked Polymer Electrolyte. *J. Electrochem. Soc* **2021**, *168*, 050549.

(22) Kim, H. K.; Barai, P.; Chavan, K.; Srinivisan, V. Transport and Mechanical Behavior in PEO-LLZO Composite Electrolytes. *J Solid State Electrochem.* **2022**, *26*, 2059−2075.

(23) Brogioli, D.; Langer, F.; Kun, R.; La Mantia, F. Space-Charge Effects at the $Li_7La_3Zr_2O_{12}$/Poly(ethylene oxide) Interfaces. *ACS Appl. Mater. Interfaces* **2019**, *11*, 11999.

(24) Cheng, Z.; Liu, M.; Ganapathy, S.; Li, C.; Li, Z.; Zhang, X.; He, P.; Zhou, H.; M. Wagemaker Revealing the Impact of Space-Charge Layers on the Li-Ion Transport in all Solid-State batteries. *Joule* **2020**, *4*, 1311−1323.

(25) An, Y.; Han, X.; Liu, Y.; Azhar, A.; Na, J.; Nanjundan, A. K.; Wang, S.; Yu, J.; Yamauchi, Y. Progress in Solid Polymer Electrolytes for Lithium-Ion Batteries and Beyond. *Small* **2022**, *18*, 2103617.

(26) Zhang, X.; Han, J.; Niu, X.; Xin, C.; Xue, C.; Wang, S.; Shen, Y.; Zhang, L.; Li, L.; Nan, C. W. High Cycling Stability for Solid-State Li Metal Batteries via Regulating Solvation Effect in Poly(Vinylidene Fluoride)-Based Electrolytes. *Batter. Supercaps* **2020**, *3*, 876−883.

(27) Choo, Y.; Halat, D. M.; Villaluenga, I.; Timachova, K.; Balsara, N. P. Diffusion and Migration in Polymer Electrolytes. *Prog. Poly. Sci.* **2020**, *103*, 101220.

(28) Yu, X.; Manthiram, A. A Review of Composite Polymer-Ceramic Electrolytes for Lithium Batteries. *Energy Storage Mater.* **2021**, *34*, 282−300.

(29) Zhang, H.; Liu, C.; Zheng, L.; Xu, F.; Feng, W.; Li, H.; Huang, X.; Armand, M.; Nie, J.; Zhou, Z. Lithium Bis(fluorosulfonyl)imide/Poly(ethylene oxide) Polymer Electrolyte. *Electrochim. Acta* **2014**, *133*, 529−538.

(30) Fong, K. D.; Self, J.; Diederichsen, K. M.; Wood, B. M.; McCloskey, B. D.; Persson, K. A. Ion Transport and the True Transference Number in Nonaqueous Polyelectrolyte solutions for Lithium Ion Batteries. *ACS Cent. Sci.* **2019**, *5*, 1250−1260.

(31) Cheng, S.; Smith, D. M.; Li, C. Y. How does Nanoscale Crystalline Structure Affect Ion Transport in Solid Polymer Electrolytes? *Macromolecules* **2014**, *47*, 3978−3986.

(32) Chen, Q.; Masser, H.; Shiau, H. S.; Liang, S.; Runt, J.; Painter, P. C.; Colby, R. H. Linear Viscoelasticity and Fourier Transform Infrared Spectroscopy of Polyether–Ester–Sulfonate Copolymer Ionomers. *Macromolecules* **2014**, *47*, 3635−3644/

(33) Stewart-Sloan, C. R.; Olsen, B. D. Protonation-Induced Microphase Separation in Thin Films of a Polyelectrolyte-Hydrophilic Diblock Copolymer. *ACS Macro Letters* **2014**, *3*, 410−414.

(34) Yang, L.; Wang, Z.; Feng, Y.; Tan, R.; Zuo, Y.; Gao, R.; Zhao, Y.; Han, L.; Wang, Z.; Pan, F. Flexible Composite Solid Electrolyte Facilitating Highly Stable "Soft Contacting" Li–Electrolyte Interface for Solid State Lithium-Ion Batteries. *Adv. Energy Mater.* **2017**, *7*, 1701437.

(35) Havriliak, S.; Negami, S. A Complex Plane Representation of Dielectric and Mechanical Relaxation Processes in Some Polymers. *Polymer* **1967**, *8*, 161−210.

(36) Kremer, F.; Schönhals A. (eds.) Broadband Dielectric Spectroscopy. Springer-Verlag, Berlin, Germany, **2002**.

(37) Polizos, G.; Tuncer, E.; Tomer, V.; Sauers, I.; Randall, C. A.; Manias, E. Dielectric Spectroscopy of Polymer-Based Nanocomposite Dielectrics with Tailored Interfaces and

Structured Spatial Distribution of Fillers, in Nanoscale Spectroscopy with Applications, Musa, S. M. ed., CRC Press, Boca Raton, FL, USA, **2013**, 93−130.

(38) Toda, A. Spherulitic Growth in Crystalline Polymers. In: Palsule, S. (eds) Encyclopedia of Polymers and Composites. **2013**, Springer, Berlin, Heidelberg.

(39) Alfonso, G. C.; Russell, T. P. Kinetics of Crystallization in Semicrystalline/Amorphous Polymer Mixtures. *Macromolecules* **1986**, *19*, 1143−1152.

(40) Goswami, M.; Iyiola, O. O.; Lu, W.; Hong, K.; Zolnierczuk, P.; Stungaciu, L. R.; Heller, W. T.; Taleb, O.; Sumpter, B. G.; Hallinan, D. T. Understanding Interfacial Block Copolymer Structure and Dynamics. *Macromolecules* **2023**, *56*, 762−771.

(41) Wang, X.; Hong, K.; Baskaran, D.; Goswami, M.; Sumpter, B. G.; Mays, J. Asymmetrical Self-Assembly from Fluorinated and Sulfonated Block Copolymers. *Soft Matter* **2011**, *7*, 7960−7964.

(42) Goswami, M.; Borreguero, J. M.; Pincus, P. A.; Sumpter, B. G. Surfactant-Mediated Polyelectrolyte Self-Assembly in a Polyelectrolyte–Surfactant Complex. *Macromolecules* **2015**, *48*, 9050−9059.

(43) Borreguero, J. M.; Pincus, P. A.; Sumpter, B. G.; Goswami, M. Dynamics of Charged Species in Ionic-Neutral Block Copolymer and Surfactant Complexes. *J. Phys. Chem. B* **2017**, *121*, 6958−6968.

(44) Polizos, G.; Sharma, J.; Jafta, C. J.; Muralidharan, N.; Veith, G. M.; Keum, J. K.; Kukay, A.; Sahore, R.; Wood III, D. L. Nanostructured Ligament and Fiber Al–Doped $Li_7La_3Zr_2O_{12}$ Scaffolds to Mediate Cathode-Electrolyte Interface Chemistry. *J. Power Sources* **2021**, *513*, 230551.

(45) Thompson, A. P.; Aktulga, H. M.; Berger, R.; Bolintineanu, D.S.; Brown, W. M.; Crozier, P. S.; in't Veld, P. J.; Kohlmeyer, A.;Moore, S. G.; Nguyen, T. D.; Shan, R.; Stevens, M. J.; Tranchida, J.;Trott, C.; Plimpton, S. J. LAMMPS - a Flexible Simulation Tool for Particle-Based Materials Modeling at the Atomic, Meso, and Continuum Scales. *Comput. Phys. Commun.* **2022**, *271*, No. 108171.

(46) Jewett, A. I.; Stelter, D.; Lambert, J.; Saladi, S. M.; Roscioni, O. M.; Ricci, M.; Autin, L.; Maritan, M.; Bashusqeh, S. M.; Keyes, T.; Dame, R. T.; Shea, J. E.; Jensen, G. J.; Goodsell, D. S. Moltemplate: A Tool for Coarse-Grained Modeling of Complex Biological Matter and Soft Condensed Matter Physics. *J. Mol. Biol.* **2021**, *433*, 166841.

(47) Schmid, N.; Eichenberger, A. P.; Choutko, A.; Riniker, S.; Winger, M.; Mark, A. E.; van Gunsteren, W. F. Definition and Testing of the GROMOS Force-Field Versions 54A7 and 54B7. *Eur. Biophys. J.* **2011**, *40*, 843−856.

(48) Jorgenson, W. L.; Maxwell, D. S.; Tirado-Rives, J. Development and Testing of the OPLS All-Atom Force Field on Conformational Energetics and Properties of Organic Liquids. *J. Am. Chem. Soc.* **1996**, *118*, 11225−11236.

(49) Shimizu, K.; Almantariotis, D.; Costa Gomes, M. F.; Padua, A. A. H.; Canongia Lopes, J. N. Molecular Force Field for Ionic Liquids V: Hydroxyethylimidazolium, Dimethoxy-2-Methylimidazolium, and Fluoroalkylimidazolium Cations and Bis(Fluorosulfonyl)Amide,

Perfluoroalkanesulfonylamide, and Fluoroalkylfluorophosphate Anions. *J. Phys. Chem. B* **2010**, *114*, 3592−3600.

(50) Muckley, E. S.; Aytug, T.; Mayes, R.; Lupini, A. R.; Carrillo, J. M. Y.; Goswami, M.; Sumpter, B. G.; Ivanov, I. N. Hierarchical TiO_2:Cu_2O Nanostructures for Gas/Vapor Sensing and CO_2 Sequestration. *ACS Appl. Mater. Interfaces* **2019**, *11*, 48466−48475.

(51) Nallet, F.; Laversanne, R.; Roux, D. Modelling X-ray or Neutron Scattering Spectra of Lyotropic Lamellar Phases: Interplay Between Form and Structure Factors. *J. Phys. II Fr.* **1993**, *3*, 487−502.

(52) Berghausen, J.; Zipfel, J.; Lindner, P.; Richtering, W. Influence of Water-Soluble Polymers on the Shear-Induced Structure Formation in Lyotropic Lamellar Phases. *J. Phys. Chem. B* **2001**, *105*, 11081−11088.

(53) Bergström, M.; Pedersen, J. S. A Small-Angle Neutron Scattering (SANS) Study of Tablet-Shaped and Ribbonlike Micelles Formed from Mixtures of an Anionic and a Cationic Surfactant. *J. Phys. Chem. B* **1999**, *103*, 8502−8513.

(54) Keum, J. K.; Burger, C.; Hsiao, B. S.; Somani, R.; Yang, L.; Chu, B.; Kolb, R.; Chen, H.; Lue, C. T. Synchrotron X-Ray Scattering Studies of the Nature of Shear-Induced Shish-Kebab Structure in Polyethylene Melt. *Progr. Colloid Polym. Sci.* **2005**, *130*, 114−126.

(55) Guinier, A.; Fournet, G. Small-Angle Scattering of X-Rays. John Wiley and Sons, New York, 1955.

(56) Percus, J. K.; Yevick, G. J. Analysis of Classical Statistical Mechanics by Means of Collective Coordinates. *Phys. Rev.* **1958**, *110*, 1.

(57) Schulz, G. Uber Die Kinetik Der Kettenpolymerisationen. *Z. Phys. Chem. B* **1939**, *43*, 25−46.

(58) Hammouda, B. A. New Guinier-Porod Model. *J. Appl. Crystallogr.* **2010**, *43*, 716−719.